

Conditionally Averaged Large-Scale Motions in the Neutral Atmospheric Boundary Layer: Insights for Aeolian Processes

Chinthaka Jacob¹ · William Anderson¹

Received: 22 December 2015 / Accepted: 7 June 2016
© Springer Science+Business Media Dordrecht 2016

Abstract Aeolian erosion of flat, arid landscapes is induced (and sustained) by the aerodynamic surface stress imposed by flow in the atmospheric surface layer. Conceptual models typically indicate that sediment mass flux, Q (via saltation or drift), scales with imposed aerodynamic stress raised to some exponent, n , where $n > 1$. This scaling demonstrates the importance of turbulent fluctuations in driving aeolian processes. In order to illustrate the importance of surface-stress intermittency in aeolian processes, and to elucidate the role of turbulence, conditional averaging predicated on aerodynamic surface stress has been used within large-eddy simulation of atmospheric boundary-layer flow over an arid, flat landscape. The conditional-sampling thresholds are defined based on probability distribution functions of surface stress. The simulations have been performed for a computational domain with $\approx 25H$ streamwise extent, where H is the prescribed depth of the neutrally-stratified boundary layer. Thus, the full hierarchy of spatial scales are captured, from surface-layer turbulence to large- and very-large-scale outer-layer coherent motions. Spectrograms are used to support this argument, and also to illustrate how turbulent energy is distributed across wavelengths with elevation. Conditional averaging provides an ensemble-mean visualization of flow structures responsible for erosion ‘events’. Results indicate that surface-stress peaks are associated with the passage of inclined, high-momentum regions flanked by adjacent low-momentum regions. Fluid in the interfacial shear layers between these adjacent quasi-uniform momentum regions exhibits high streamwise and vertical vorticity.

Keywords Aeolian processes · Aerodynamic stress · Conditional averaging · Large-eddy simulation · Large-scale motions · Structural inclination

✉ William Anderson
wca140030@utdallas.edu

¹ Mechanical Engineering Department, University of Texas at Dallas, Richardson, TX, USA

1 Introduction

Turbulent mixing in the Earth's atmospheric boundary layer (ABL) is important in a variety of fields: from air quality and dispersion processes in urban environments (Bohm et al. 2000; Cheng and Castro 2002; Coceal et al. 2007; Harmon and Finnigan 2007; Xie et al. 2008; Belcher et al. 2012; Anderson et al. 2015); to pollen transport and aerodynamics of plant canopies (Chester et al. 2007; Finnigan et al. 2009; Belcher et al. 2012; Bai et al. 2012; Graham and Meneveau 2012; Bailey and Stoll 2013); economics of wind farm management (Calaf et al. 2010, 2011); and aeolian erosion and dust emissions from arid landscapes (Anderson and Chamecki 2014). In the absence of a vertical thermal gradient¹, the horizontally homogeneous ABL surface layer is composed of a roughness sublayer and inertial (logarithmic) layer. The roughness sublayer depth, z_{RSL} , scales linearly with aggregate obstacle height, h , where $2 \lesssim z_{RSL}/h \lesssim 5$ is a commonly-cited range (Grass 1971; Raupach et al. 1991; Jimenez 2004; Castro 2007; Schultz and Flack 2009). In the inertial sublayer above, however, provided $H/h \gtrsim 40$ (where H is the boundary-layer depth), Townsend's hypothesis states that a scale separation exists in which the outer-layer flow exhibits a universality that is independent of the roughness sublayer (with the exception of its response to the friction velocity, u_* , and H ; Townsend 1976; Jimenez 2004).

For a 'typical' ABL depth of, say, $H \approx 1000$ m, and adopting $H/h = 40$ as a condition for outer-layer similarity, $h \approx 25$ m; as a cursory assumption, one could further adopt the model $z_0 \approx 0.1h$ (Garratt 1994), which would indicate $z_0 \lesssim 2.5$ m for outer-layer similarity. Comparison of this value against 'textbook' roughness lengths (Brutsaert 2005) indicates that many landscapes are not so rough that outer-layer similarity is inhibited via attenuation of inertial layer correlation (Krogstad et al. 1992; Krogstad and Antonia 1999; Wu and Christensen 2007, 2010). Thus, the inertial layer of the ABL is occupied by large- and very-large-scale motions transporting substantial turbulent kinetic energy (Klewicki et al. 1995; Hutchins and Marusic 2007a; Fang and Porté-Agel 2015). In rough-wall turbulence, large-scale motions are flanked by counter-rotating streamwise vorticity and encapsulated by hairpin vortices (Ganapathisubramani et al. 2003; Hutchins and Marusic 2007a; Volino et al. 2007; Hong et al. 2012) associated with interfacial shear layers separating adjacent relatively high-momentum fluid regions (Meinhart and Adrian 1995). Further, large-scale motions and very-large-scale motions spatially meander in the $x-y$ plane, which complicates evaluation of their characteristic scale based on two-point correlations of fluctuating velocity (Hutchins and Marusic 2007a).

The presence of large- and very-large-scale motions in turbulent boundary-layer flow, pipe flow, and channel flow has received significant interest. And recent smooth-wall experiments have demonstrated that these structures play an important role on the dynamics of the inner, viscous-affected region (Mathis et al. 2009; Marusic et al. 2010; Mathis et al. 2011). That is, large- and very-large-scale motions are positively correlated with small-scale dynamics of the near-wall region. For rough wall flows at ABL-scale Reynolds numbers, Anderson (2015) recently demonstrated that an analogous modulation is present between the inertial layer and roughness sublayer. If large- and very-large-scale motions are positively correlated with roughness sublayer dynamics, and since roughness sublayer dynamics set the friction velocity via $u_* = \max(\langle u' w' \rangle_{x,y,t}^{1/2})$, it is of fundamental importance to discern their influence on the imposed aerodynamic surface stress (where superscript 'prime' denotes deviations

¹ In this study, $\mathbf{x} = \{x, y, z\}$ corresponds with the streamwise, transverse, and vertical directions respectively. $\mathbf{u} = \{u, v, w\}$ corresponds with the streamwise, transverse, and vertical velocity components, respectively, and it is emphasized that the annotations for time averaging or spatial averaging of velocity are not introduced here for simplicity.

from a homogeneous dimension and $\langle \cdot \rangle_a$ denotes averaging over dimension a). Indeed, it is known that surface stress, τ^w , is intermittent (Grant and Marusic 2012; Mathis et al. 2013). Here, we investigate how the dynamics of ABL turbulence affect surface-stress intermittency and, thus, how this drives aeolian activity of arid landscapes. Large-eddy simulation (LES) was used to model neutrally-stratified ABL flow over a flat landscape with aerodynamic roughness length, z_0 , set to a value representative of an arid landscape (limited vegetation). The prevailing hypothesis is that large- and very-large-scale motions are present during extreme values of surface stress, and this is important for characterizing spatial patterns of erosion due to the passage of these structures. This work is compelled by efforts to associate turbulent dynamics with aeolian processes: wind-driven mobilization of dust and sediment.

1.1 Aeolian Morphodynamics

During periods of aeolian activity, turbulence exerts aerodynamic forces that can mobilize stationary sediment grains such that they are dislodged from the sandy surface. In a mode of transport known as ‘saltation’, sediment grains are briefly suspended in a ballistic trajectory in response to surface (aerodynamic drag) and body forces (gravity). Upon impact, sediment grains perpetuate aeolian saltation by ‘splashing’ other grains from the sediment bed (Shao 2008; Kok et al. 2012; Pahtz et al. 2012). Models of aeolian saltation mass transport, Q , are typically based upon a power-law scaling with friction velocity, $Q \sim u_*^n$ (Kok et al. 2012; Martin et al. 2013), where $n = 3$ is commonly reported. For example, consider the Bagnold scheme (Bagnold 1937, 1956; Kok et al. 2012; Martin et al. 2013),

$$Q = C_B \left(\frac{D_p}{D_{250}} \right)^{1/2} \frac{\rho_a}{g} u_*^3, \quad (1)$$

where $C_B \sim \mathcal{O}(10^0)$ is a dimensionless empirical parameter, ρ_a is the density of air, D_p is the aggregate particle diameter, $D_{250} = 250 \mu\text{m}$ is a reference particle diameter, and g is acceleration due to gravity [the efficacy of Eq. 1-style relations is itself an open question, see (Kok et al. 2012; Martin et al. 2013)]. Thus, since $u_* \sim u'$, and $Q \sim u_*^n$, one concludes that turbulent momentum transport could be crucially important in the mobilization of dust and sediment. Moreover, the friction velocity developed by the neutrally-stratified ABL imposed pressure gradient forcing, dP_∞/dx , is,

$$u_* = \left(\frac{\tau^w}{\rho_a} \right)^{1/2} = \left(- \frac{dP_\infty}{dx} \frac{H}{\rho_a} \right)^{1/2}, \quad (2)$$

where dP_∞/dx can be readily defined in terms of geostrophic conditions in the ABL based on the time homogeneous and horizontally homogeneous momentum balance (Wyngaard 2010). The limiting stress required to initiate grain mobilization via aeolian saltation is defined by the so-called ‘threshold’ friction velocity, $u_{*,t}$, where empirical correlations parametrize $u_{*,t}$ via grain properties, vegetation density, and soil moisture content (Shao 2008). The Bagnold scheme is a commonly used empirical relation for $u_{*,t}$ (Bagnold 1956; Shao 2008; Kok et al. 2012),

$$u_{*,t} = A_B \left(\frac{\rho_p}{\rho_a} g D_p \right)^{1/2}, \quad (3)$$

where $A_B = A_B(Re_{*,t}) \sim \mathcal{O}(10^{-1})$ is a non-dimensional coefficient related to the particle shear threshold velocity, $Re_{*,t} = u_{*,t} D_p / v$, and ρ_p is sand grain density. In order to reconcile

ABL forcing with aeolian morphodynamics, a new ratio is defined in terms of Eqs. 2 and 3,

$$\lambda = \frac{u_*}{u_{*,t}} = A_B^{-1} \left(-\frac{dP_\infty}{dx} \frac{H}{\rho_p g D_p} \right)^{1/2}. \quad (4)$$

Equation 4 is a non-dimensional indicator of aeolian activity under the prevailing atmospheric conditions. Practically, however, it is more convenient to define u_* in terms of ambient streamwise geostrophic speed, U_G , at the top of the surface layer (Tennekes and Lumley 1972),

$$u_* = \kappa U_G \left[\ln \left(\frac{H_G}{z_0} \right) \right]^{-1}, \quad (5)$$

where H_G is the surface-layer depth and κ is the von Kármán constant. Equation 5 allows the non-dimensional threshold, λ (Eq. 4), to be defined alternatively as,

$$\lambda = \frac{u_*}{u_{*,t}} = \kappa U_G \left[A_B \ln \left(\frac{H_G}{z_0} \right) \right]^{-1} \left(\frac{\rho_p}{\rho_a} g D_p \right)^{-1/2}. \quad (6)$$

It follows that the prevailing conditions responsible for setting the ABL value of u_* are critically important to aeolian activity. In the absence of sufficiently strong dP_∞/dx , $\lambda < 1$ and aeolian saltation would occur only intermittently due to turbulent variations in u_* (Lanigan et al. 2015). And in the context of anthropogenic or paleoenvironmental landscape degradation in a process known as ‘desertification’ (Thomas et al. 2005; Reynolds et al. 2007; Dupont et al. 2015), aeolian saltation would occur more readily with declining vegetative cover and moisture content as its $u_{*,t}$ reduces.

1.2 Present Study

In this study, LES was used to model ABL turbulence in a domain with streamwise extent, $L_x/H = 8\pi$, where $H = 1000$ m is the prescribed boundary-layer depth; the computational mesh set-up is sketched in Fig. 1. The domain was thus adequately long to resolve large- and very-large-scale motions present in the domain, and spectrograms of fluctuating resolved streamwise velocity to support this claim. Moreover, a time series of aerodynamic surface stress at one point on the rough surface was recorded over $U_0 T H^{-1} \sim \mathcal{O}(10^4)$ large-eddy turnovers (Hutchins et al. 2009), and used this to generate a probability distribution function (p.d.f.) of surface stress that provides guidance on the statistics of stress intermittency and the probability of extreme conditions. Informed by the p.d.f., additional simulations were made to conditionally sample the flow based on pre-defined threshold exceedance of surface stress, thereby attaining flow characteristics associated with extreme stress (i.e. instances associated with mobilization of sediment via aeolian processes). The results indicate that large- and very-large-scale motions are present during stress extremes, which is important given their spatial footprint². In Sect. 3.3, candidate values for $u_{*,t}$ and u_* (recall Sect. 1.1)—based on values typical of an arid, flat landscape—are used to demonstrate that the conditionally-averaged stress is indeed associated with the presence of large- and very-large-scale motions. This work is not without precedent: in a recent direct numerical simulation study of turbulent Couette flow (Richter and Sullivan 2014), conditional averaging was used to explore turbulence structural attributes during extreme flow events (for a flow that was transporting inertial particles). Meanwhile, others have investigated the role of near-surface coherent structures in dust transport (Baas 2006, 2008). Section 2 provides a brief description

² Here, footprint refers to the spatial extent of coherent motions (Hutchins and Marusic 2007b).

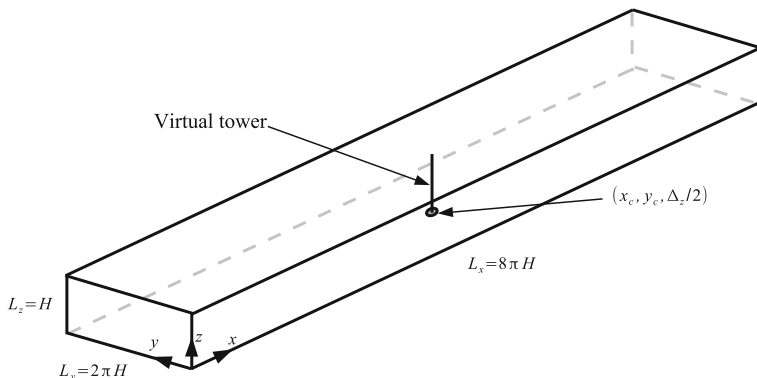


Fig. 1 Sketch of computational domain for present simulations with annotation of stress sampling point $(x_c, y_c, \Delta z/2)$ and position of virtual tower used for generating time series datasets

Table 1 Summary of simulation attributes ($H = 1000$ m)

Case	N_x	N_y	N_z	L_x/H	L_y/H	L_z/H	z_0/H	$\delta_t u_* H^{-1}$	TU_0/H
LES1	256	64	64	8π	2π	1	5×10^{-6}	9.0×10^{-5}	12350
LES2	384	96	96	8π	2π	1	5×10^{-6}	7.2×10^{-5}	3750
LES3	512	128	128	8π	2π	1	5×10^{-6}	6.3×10^{-5}	3213

of the LES code and cases, and results of the LES and conditional sampling procedure are given in Sect. 3. Concluding remarks are given in Sect. 4.

2 Methods

The LES code solves the momentum transport equation for evolution of $\tilde{\mathbf{u}}(\mathbf{x}, t)$ under incompressible, $\nabla \cdot \tilde{\mathbf{u}}(\mathbf{x}, t) = 0$, and high Reynolds number, $\nu \nabla^2 \tilde{\mathbf{u}}(\mathbf{x}, t) = 0$, conditions for $\mathbf{x} \in \Omega$ and $t > 0$. The code used here is a version of the “JHU-LES” code, originally presented in Albertson and Parlange (1999). The vertical extent of the domain embodies the ABL surface layer and outer layer, although it is emphasized that Coriolis accelerations are not included in the momentum transport solver. Note that $\tilde{\cdot}$ denotes a grid-filtered (LES) quantity (Meneveau and Katz 2000). Incompressibility is preserved by computing the divergence of the momentum transport equation, $\nabla \cdot [D\tilde{\mathbf{u}}/Dt = \nabla \cdot \boldsymbol{\sigma}]$, which yields a pressure Poisson equation that is solved to evaluate the pressure gradient that sustains a solenoidal velocity field. Spatial details of the computational domain, Ω , are defined in Table 1, where the streamwise extent, $L_x/H = 8\pi$, is selected to capture large- and very-large-scale motions (Hutchins and Marusic 2007a; Volino et al. 2007; Fang and Porté-Agel 2015). The momentum transport equation is forced by an imposed streamwise pressure gradient (Eq. 2, where $(-\partial P_\infty / \partial x_{pa})^{1/2} = -1$), which sets the friction velocity, u_* , upon which all velocities are scaled. Table 1 also shows the shear-normalized timestep, $\delta_t u_* H^{-1}$. Owing to pseudo-spectral discretization in the horizontal directions, periodic boundary conditions are imposed on the vertical planes of the domain; channel centreline conditions are imposed on the top

boundary with the zero-stress, $\partial\tilde{u}/\partial z|_H = \partial\tilde{v}/\partial z|_H = 0$, and zero-penetration conditions, $\tilde{w}|_H = 0$ (Albertson and Parlange 1999; Anderson and Meneveau 2010, 2011; Stevens et al. 2014). These top boundary conditions replicate the effects of the ambient capping inversion, which inhibits continual thickening of the flow (Deardorff 1972; Wyngaard 1979; Moeng 1984; Mason and Thomson 1987). Table 1 shows the domain length and number of computational mesh points, where $\delta x = L_x/N_x$, $\delta y = L_y/N_y$ and $\delta z = H/N_z$. Surface boundary conditions are implemented with the equilibrium logarithmic law,

$$\tau_{xz}^w(x, y, t) = - \left[\frac{\kappa U(x, y, t)}{\ln(\frac{1}{2}\delta z/z_0)} \right]^2 \frac{\bar{\tilde{u}}(x, y, \delta z/2, t)}{U(x, y, t)} \quad (7)$$

and

$$\tau_{yz}^w(x, y, t) = - \left[\frac{\kappa U(x, y, t)}{\ln(\frac{1}{2}\delta z/z_0)} \right]^2 \frac{\bar{\tilde{v}}(x, y, \delta z/2, t)}{U(x, y, t)} \quad (8)$$

where $\kappa = 0.4$, z_0 is summarized in Table 1, and $U(x, y, t) = [\bar{\tilde{u}}(x, y, \delta z/2, t)^2 + \bar{\tilde{v}}(x, y, \delta z/2, t)^2]^{1/2}$ is the magnitude of the test-filtered horizontal components of velocity, where test-filtering is denoted by $\bar{\cdot}$ (Germano et al. 1991; Germano 1992). A value of $z_0/H = 5 \times 10^{-6}$ was used for the present simulations (see also Table 1), which was selected to match conditions on a dry, flat, minimally-vegetated landscape (Brutsaert 2005). Test-filtering attenuates the velocity variance at elevation $\delta z/2$, and provides a means to evaluate surface stress based on large-scale features of the flow, absent “peaks” that would result in excessively large surface stress via Eqs. 7 and 8 (Bou-Zeid et al. 2005). Subgrid-scale stresses are modelled with an eddy-viscosity model, $\tau^d = -2\nu_t S$, where $S = \frac{1}{2}(\nabla u + \nabla u^T)$ is the resolved strain-rate tensor. The eddy viscosity is $\nu_t = (C_s \Delta)^2 |S|$, where $|S| = (2S:S)^{1/2}$, C_s is the Smagorinsky coefficient, and Δ is the grid resolution. For the present simulations, the Lagrangian scale-dependent dynamic model is used (Bou-Zeid et al. 2005). This closure is based on averaging over fluid pathlines, which removes the need to assume turbulence horizontal statistical homogeneity [as would otherwise be required with earlier subgrid-scale closures, (Germano et al. 1991)].

3 Results and Discussion

The aforementioned LES code was solved for the computational domain sketched in Fig. 1 and with attributes summarized in Table 1. The code was solved with the resolutions indicated in Table 1, which provides a means to identifying how observations of extreme stress vary with resolution. The domain length ensures that large- and very-large-scale motions are resolved, as shown below with spectrograms of the resolved fluctuating streamwise velocity component (Hutchins and Marusic 2007a). In the following series of subsections, it is first qualitatively demonstrated that the full hierarchy of spatial lengths is resolved in the simulations. This is used to discuss surface-stress fluctuations and conditional averaging, all of which culminates in demonstration that large- and very-large-scale motions are present when surface stress exhibits extreme values. The results on surface stress are discussed in the context of actual, physically realistic values of aeolian threshold friction velocity, which broadens the applicability of findings from this study.

3.1 Instantaneous Quantities

For qualitative indication of this, Fig. 2 shows instantaneous visualization of the fluctuating streamwise velocity, $\tilde{u}' = \tilde{u} - \langle \tilde{u} \rangle_{x,y}$, where $\langle \cdot \rangle_{x,y}$ denotes plane averaging (hereafter, superscript ‘prime’ denotes deviation from horizontal plane-average). Figure 2a shows an $x - z$ transect of \tilde{u}' at transverse position, $y/H = \pi$. To this contour, red lines at the interfaces between regions of quasi-uniform momentum were added; the lines are inclined at $\theta = 15^\circ$, the commonly reported structural inclination angle (Hutchins et al. 2012; Chauhan et al. 2013) of large-scale motions composed of low- or high-momentum fluid (so-called low- and high-momentum regions, respectively). It is emphasized that both low- and high-momentum regions exhibit inclination angles in agreement with reported literature values (Anderson et al. 2015), while observed quasi-uniform momentum region lengths are similar and comparable to the often-reported $\approx 3H$ of large-scale motions (for example, low-momentum regions are present for $2.5 \lesssim x/H \lesssim 6$ and $14.8 \lesssim x/H \lesssim 18$, while high-momentum regions are present for $6 \lesssim x/H \lesssim 8$ and $10 \lesssim x/H \lesssim 14$; see (Hutchins and Marusic 2007a)). The streamwise extent of a very-large-scale motion is often reported as $\approx 20H$ (Kim and Adrian 1999; Balakumar and Adrian 2007; Dennis and Nickels 2011a, b; Ahn et al. 2015), and it is argued here that very-large-scale motions occur via streamwise coalescence of large-scale motions (although both structures are resolved in the present simulations).

Figure 2b is an $x - y$ contour of instantaneous \tilde{u}' at elevation, $z/H = 0.0742$. For discussion, a red line has been added to highlight the silhouette of a very-large-scale motion (in this case, composed of a relative momentum deficit). The very-large-scale motion boundaries were subjectively defined by the authors and, indeed, the selected very-large-scale motion was one of many that could have been highlighted (Fang and Porté-Agel 2015). The

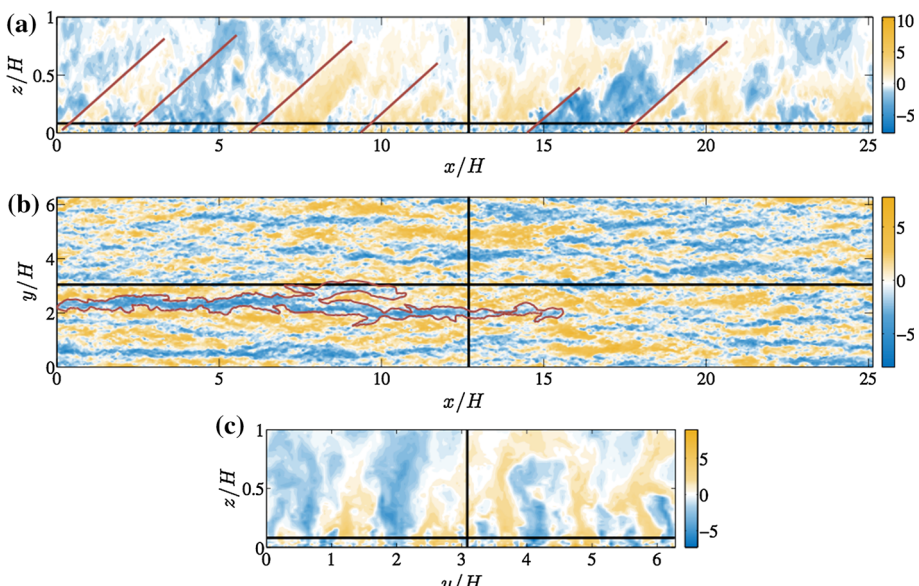


Fig. 2 Visualization of instantaneous fluctuating streamwise velocity component, $\tilde{u}'(x, y, z, t)/u_*$, in: **a** $x - z$ plane at transverse position, $y/H = \pi$; **b** $x - y$ plane at elevation, $z/H \approx 0.075$; and **c** $y - z$ plane at streamwise position, $x/H = 4\pi$. Red line added on panel **a** denotes $\theta = 15^\circ$ structural inclination angle (Chauhan et al. 2013). Red line on panel **b** denotes silhouette of very-large-scale motion

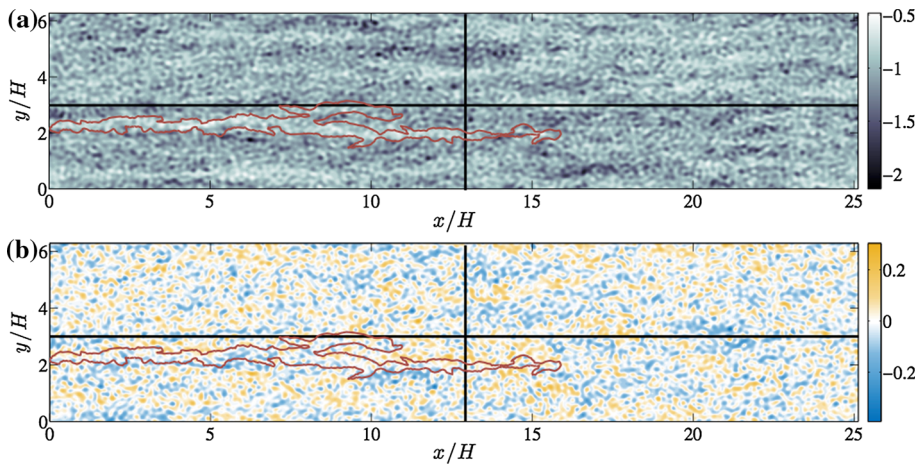


Fig. 3 Visualization of instantaneous aerodynamic surface stress corresponding with the flow field shown in Fig. 2: **a** $\tau_{xz}^w(x, y, t)/u_*^2$; and **b** $\tau_{yz}^w(x, y, t)/u_*^2$. Red line is added to denote silhouette of very-large-scale motion

purpose of this exercise is simply to demonstrate that, at any given time, large structures (i.e. exceeding H) are present and these structures affect turbulence statistics. The meandering, streaky nature of this structure is entirely consistent with previous observations of very-large-scale motions (Hutchins and Marusic 2007a; Fang and Porté-Agel 2015). More striking is the apparent ‘patchwork’ of uniform momentum regions of alternating sign, separated by interfacial shear layers (Hutchins et al. 2011). Finally, Fig. 2c shows an instantaneous contour of \tilde{u}' in the $y-z$ plane at $x/H = 4\pi$. The figure shows turbulent plumes of low- and high-momentum fluid occupying the depth of the channel, as would be expected. Low-momentum regions are flanked by counter-rotating vortices with positive and negative sign on their ‘left’ and ‘right’ sides; this will be further shown below in the conditionally-sampled fields.

Figure 3a, b shows instantaneous contours of the $x-z$ (Eq. 7) and $y-z$ (Eq. 8) components of surface stress, respectively. τ_{xz}^w and τ_{yz}^w are shown at the same instant as that associated with Fig. 2, which enables qualitative association of the surface stress and flow field. Indeed, the red silhouette from Fig. 2b is superimposed on Fig. 3a and b. It is self-evident that stress magnitude should be correlated with momentum excesses and deficits, given use of the logarithmic law (Eqs. 7 and 8). The spatial footprint of large- and very-large-scale motions is clearly visible in the stress contours, which supports underlying arguments that surface stress variability is present and must be important for aeolian processes. Note finally that the red silhouette on the Fig. 3b τ_{yz}^w contour generally overlaps with locations where τ_{yz}^w exhibits largest (magnitude) values of alternating sign. That is, sections of the silhouette along the ‘top’ and ‘bottom’ (with respect to y/H) correspond with $\tau_{yz}^w > 0$ and $\tau_{yz}^w < 0$, respectively. Since τ_{yz}^w is negatively correlated with \tilde{v} by virtue of the logarithmic law (Eq. 8), locations of $\tau_{yz}^w > 0$ and $\tau_{yz}^w < 0$ correspond with $\tilde{v} < 0$ and $\tilde{v} > 0$, respectively. Thus, the very-large-scale motion highlighted is flanked by a ‘lateral inflow’ region at the base. This result is consistent with existing theory on dynamics of large- and very-large-scale motions, which has shown that these structures are flanked by counter-rotating streamwise vortices (wherein the sign corresponds with lateral inflow and outflow at the bottom and top, respectively) (Hutchins and Marusic 2007a; Wu and Christensen 2010).

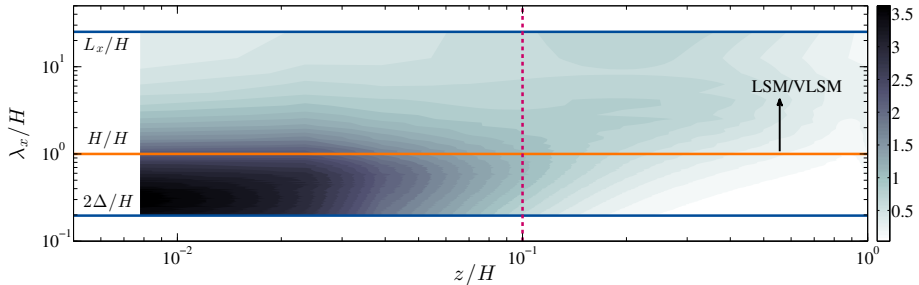


Fig. 4 Pre-multiplied energy spectrum of fluctuating streamwise velocity component for case LES1, where the colour bar shows $k_x E_{\tilde{u}'\tilde{u}'} / u_*^2$. Figure includes annotations of key geometric scales associated with problem: horizontal blue lines denote domain extent (L_x) and grid resolution (Δ), while horizontal line denotes domain depth, H . Vertical orange line denotes $z/H = 0.1$, or the elevation above which large-scale content associated with large- and very-large-scale motions should be present (Fang and Porté-Agel 2015)

3.2 Spectrogram

To comprehensively demonstrate the presence of large- and very-large-scale motions, a spectrogram of fluctuating resolved velocity, $k_x E_{\tilde{u}'\tilde{u}'} / u_*^2$, is presented in Fig. 4. These figures are illuminating, since they demonstrate how turbulent energy at different elevations is distributed across wavelengths. This view of the turbulence is fundamental to establishing the existence of ‘inner-outer’ feedbacks (Hutchins and Marusic 2007a; Mathis et al. 2009, 2011; Marusic et al. 2010; Anderson 2015) in high Reynolds number wall turbulence. Annotations are added to Fig. 4, denoting the LES grid-filter width, domain depth, and domain streamwise extent. The surface-layer depth, $z/H = 0.1$, is also annotated. The energy content primarily resides in the surface layer ($z/H \lesssim 0.1$ and $2\Delta/H < \lambda_x/H \lesssim 1$), owing to elevated turbulence-producing velocity gradients in this region. However, as has already been well reported, the signature of large- and very-large-scale motions is also apparent in the outer layer, $z/H \approx 0.2$, and annotations to demonstrate have been added. That is, there is a ‘plateau’ and ‘second mound’ in $k_x E_{\tilde{u}'\tilde{u}'} / u_*^2$ at wavenumbers exceeding $\lambda_x/H \gtrsim 10$, which is the signature of turbulence-producing very-large-scale motions. Recently, Fang and Porté-Agel (2015) use domains with streamwise extent, $L_x/H = 32\pi$, which captures the full outer peak while here the comparatively shorter domain resolves the beginning of the outer peak. This is adequate for the present purposes, and reduces the computational demand needed for running simulations of duration, $TU_0 H^{-1} \sim \mathcal{O}(10^4)$ (necessary for conditional averaging, as discussed in Sect. 3). Further, it is argued that large-scale motions, which are resolved in the domain, represent the ‘building blocks’ of very-large-scale motions [in accordance with (Kim and Adrian 1999; Balakumar and Adrian 2007; Dennis and Nickels 2011a,b; Ahn et al. 2015; Hellström et al. 2015; Anderson 2015)]. Thus, since large-scale motions are resolved, they embody the physics imparted by very-large-scale motions since the latter form via quasi-streamwise coalescence of the former.

3.3 Surface Stress and Conditional Averaging

To further this discussion, Fig. 5 shows time series of $\tilde{u}(x_c, y_c, \frac{3}{2}\delta z, t)/u_*$ and $\tau_{xz}^w(x_c, y_c, t)/u_*^2$ from position $\{x_c, y_c\}$ on Fig. 1. Velocity at elevation $\frac{3}{2}\delta z$ is shown here, since it embodies the large scale characteristics of the flow (associated with large- and very-large-scale motions) while velocity fluctuations are somewhat smaller than at $\frac{1}{2}\delta z$. So,

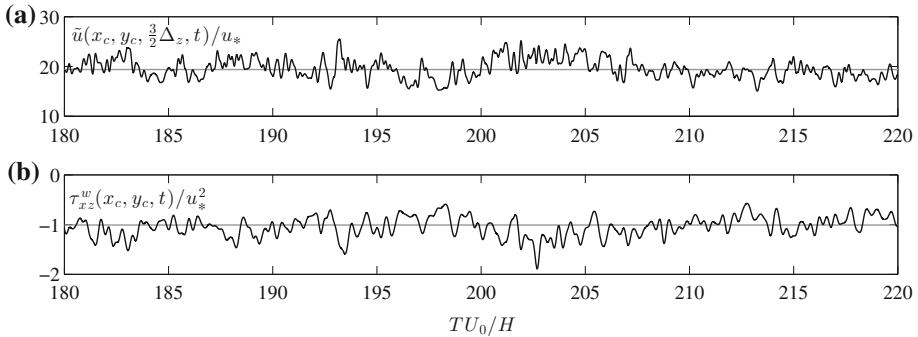


Fig. 5 Time series of aerodynamic quantities from simulation LES3. Panel **a** shows $\tilde{u}(x_c, y_c, \frac{3}{2}\delta z, t)/u_*$; panel **b** shows $\tau_{xz}^w(x_c, y_c, t)/u_*^2$. The *horizontal grey line* on both denotes a time average of quantity

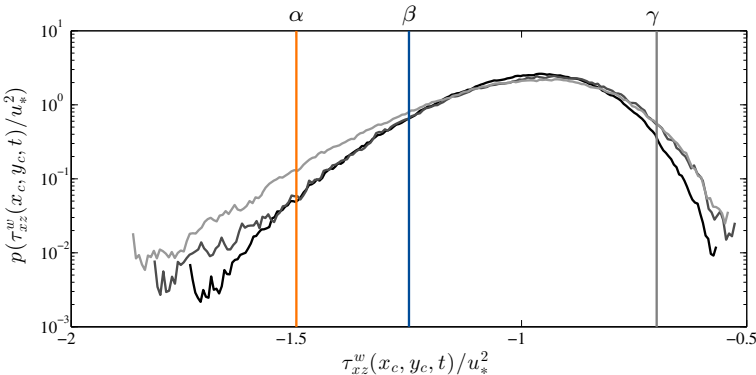


Fig. 6 Probability distribution functions of surface stress for simulations LES1 (black), LES2 (dark grey), and LES3 (light grey). Note annotation of threshold stresses: α (vertical orange line); β (vertical blue line); γ (vertical grey line)

this figure facilitates the present discussion by illustrating the correlation between velocity and surface stress magnitude. It is emphasized also that for case LES3, $\delta z/H = 0.0078$. The apparent correlation between magnitude of $\tilde{u}(x_c, y_c, \frac{3}{2}\delta z, t)/u_*$ and magnitude of $\tau_{xz}^w(x_c, y_c, t)/u_*^2$ is clear in a temporal sense, which is simply a manifestation of the underlying use of the logarithmic law (Eqs. 7 and 8). The topic of relevance here is temporal variability of $\tau_{xz}^w(x_c, y_c, t)/u_*^2$, the domain-scale flow processes responsible for such variability, and the importance of this in the context of aeolian processes. If a given landscape has threshold, $u_{*,t}$, exceeding the mean value developed by the ABL, only intermittent turbulent fluctuations could supply the momentum needed to establish aeolian saltation (discussion to follow in Sect. 1.1). Very long time-series measurements of $\tau_{xz}^w(x_c, y_c, t)/u_*^2$ were recorded for the three resolutions (LES1, LES2, and LES3, as per Table 1) and generated the p.d.f. shown in Fig. 6. The distributions show that local stress is negatively skewed, owing to intermittent high-stress events. Interestingly, one notes the subtle effect of resolution on capturing extreme stresses wherein the probability of resolving a given extreme event increases monotonically with resolution (close inspection shows that the opposite is true of the mean stress). The p.d.f.s were used to inform choices of threshold for implementation in a conditional sampling routine. Figure 6 shows the values, $\alpha = -1.5$, $\beta = -1.25$, and

$\gamma = -0.7$, where $p(\tau_{xz}^w(x_c, y_c, t)/u_*^2 \leq \alpha) \approx 10\%$, $p(\tau_{xz}^w(x_c, y_c, t)/u_*^2 \leq \beta) \approx 70\%$, and $p(\tau_{xz}^w(x_c, y_c, t)/u_*^2 \geq \gamma) \approx 50\%$. These pre-defined thresholds were used to conditionally sample the flow, *viz.*

$$\frac{\hat{\tilde{u}}_\alpha(x, y, z)}{u_*} = \left\langle \frac{\tilde{u}(x, y, z, t)}{u_*} \mid \frac{\tau_{xz}^w(x_c, y_c, t)}{u_*^2} \leq \alpha \right\rangle_{N_\alpha}, \quad (9)$$

$$\frac{\hat{\tilde{u}}_\beta(x, y, z)}{u_*} = \left\langle \frac{\tilde{u}(x, y, z, t)}{u_*} \mid \frac{\tau_{xz}^w(x_c, y_c, t)}{u_*^2} \leq \beta \right\rangle_{N_\beta}, \quad (10)$$

and

$$\frac{\hat{\tilde{u}}_\gamma(x, y, z)}{u_*} = \left\langle \frac{\tilde{u}(x, y, z, t)}{u_*} \mid \frac{\tau_{xz}^w(x_c, y_c, t)}{u_*^2} \geq \gamma \right\rangle_{N_\gamma}, \quad (11)$$

where N_α is the number of instances at which the threshold, $\tau_{xz}^w(x_c, y_c, t)/u_*^2 \leq \alpha$, is exceeded, and $\langle \cdot \rangle_{N_\alpha}$ denotes averaging over N_α instances [(the same averaging procedure is applied in Eqs. 10 and 11; (Antonia 1981; Kim et al. 1987; Adrian 1988; Sheng et al. 2009; Finnigan et al. 2009; Hutchins et al. 2011; Richter and Sullivan 2014)]. The surface stress was also conditionally sampled,

$$\frac{\hat{\tau}_{\alpha,xz}^w(x, y)}{u_*^2} = \left\langle \frac{\tau_{xz}^w(x, y, t)}{u_*^2} \mid \frac{\tau_{xz}^w(x_c, y_c, t)}{u_*^2} \leq \alpha \right\rangle_{N_\alpha}, \quad (12)$$

$$\frac{\hat{\tau}_{\beta,xz}^w(x, y)}{u_*^2} = \left\langle \frac{\tau_{xz}^w(x, y, t)}{u_*^2} \mid \frac{\tau_{xz}^w(x_c, y_c, t)}{u_*^2} \leq \beta \right\rangle_{N_\beta}, \quad (13)$$

and

$$\frac{\hat{\tau}_{\gamma,xz}^w(x, y)}{u_*^2} = \left\langle \frac{\tau_{xz}^w(x, y, t)}{u_*^2} \mid \frac{\tau_{xz}^w(x_c, y_c, t)}{u_*^2} \geq \gamma \right\rangle_{N_\gamma}. \quad (14)$$

Thus, the flow fields $\hat{\tilde{u}}_\alpha(x, y, z)$, $\hat{\tilde{u}}_\beta(x, y, z)$, and $\hat{\tilde{u}}_\gamma(x, y, z)$, provide an ensemble-mean view of the flow during local surface stress events that may be important for mobilizing sediment (Shao 2008; Kok et al. 2012; Pahtz et al. 2012). In Sect. 3, statistics of the conditionally-sampled flow field (and aerodynamic stress distribution) are shown to demonstrate that large- and very-large-scale motions are present for the selected thresholds.

3.4 Conditionally-Averaged Surface Stress

Figure 7 shows spatial ($x - y$) distributions of the conditionally-sampled surface-stress distributions (Eqs. 12, 13, and 14). For the thresholds associated with higher drag (Fig. 7a, b), the footprint of spatial variability in the flow during stress peaks is apparent. Specifically, the high stress region (proximal to the sampling point, $\{x_c, y_c\} = \{L_x/2, L_y/2\}$) is not an isolated point but is an ellipsoidal region ($10 \lesssim x/H \lesssim 14$ and $3 \lesssim y/H \lesssim 3.4$). Since the stress peak occurs over a region, as opposed to an isolated point, it indicates that coherent parcels of uniform momentum parcels are present during high stress [while the aforementioned $10 \lesssim x/H \lesssim 14$ streamwise extent agrees closely with the commonly-cited length scale of low- and high-momentum large-scale motions; (Kim and Adrian 1999; Ganapathisubramani et al. 2003; Volino et al. 2007)]. Note also that the high stress region is laterally flanked by relatively low-stress bands ($y/H \approx 1.5$ and 5.25) with significant streamwise extent. Thus, high-momentum regions above the sampling site are laterally flanked by momentum deficit regions, and this transverse variability is responsible for seconding mixing (streamwise vorticity with positive and negative sign, respectively, in the interfacial regions at $y/H \approx 4$ and 2). One notes that the $\hat{\tau}_{\beta,yz}^w(x, y)/u_*^2$ contour (Fig. 7b) is far smoother than the $\hat{\tau}_{\alpha,yz}^w(x, y)/u_*^2$

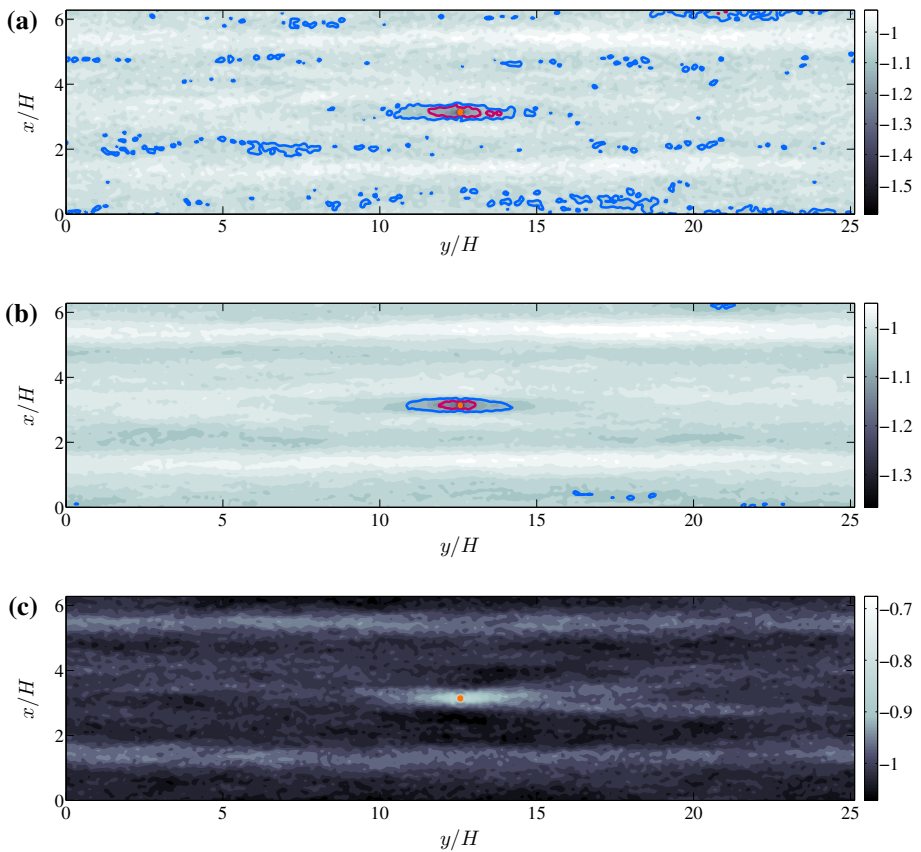


Fig. 7 Contours of conditionally-sampled aerodynamic surface stress, $\hat{\tau}_{xz}^w/u_*^2$, corresponding with thresholds illustrated in Fig. 6: **a** $\hat{\tau}_{\alpha,xz}^w(x, y)/u_*^2$; **b** $\hat{\tau}_{\beta,yz}^w(x, y)/u_*^2$; and **c** $\hat{\tau}_{\gamma,yz}^w(x, y)/u_*^2$. Orange marker denotes location of threshold stress, $\{x_c, y_c\}$, and contours correspond with case LES3 in Table 1. On panels **a** and **b**, solid blue and red contours correspond with candidate values of non-dimensional threshold stress, $u_*^2 \lambda^{-2} = 1.05$ and $u_*^2 \lambda^{-2} = 1.108$, respectively

contour (Fig. 7a), and is an outcome of the selected thresholds, since $p(\hat{\tau}_{\beta,yz}^w(x, y)/u_*^2) > p(\hat{\tau}_{\alpha,yz}^w(x, y)/u_*^2)$ (Fig. 6). Thus, $N_\alpha < N_\beta$ (fewer ensembles over which averaging can be performed).

In contrast, the conditionally-sampled low stress contour, $\hat{\tau}_{\gamma,yz}^w(x, y)/u_*^2$, is shown in Fig. 7c (recall the value of γ from the p.d.f. in Fig. 6). The distribution clearly shows a region of similar spatial extent to that reported for momentum excesses (Fig. 7a, b), with an ellipsoidal low-stress distribution centred around the sampling point (orange marker on Fig. 7 panels). That is, the spatial footprint of large-scale flow processes responsible for extreme low stress is of similar scale to that for extreme high stress. Moreover, the low-stress region is laterally flanked by two relatively high-stress bands, and a low-stress region downwind of the sampling point appears to spread laterally with downstream distance. This is associated with secondary flow processes in the interfacial region between adjacent regimes of momentum excess and deficit (Sheng et al. 2009); additional discussion to follow, below. To advance this discussion,

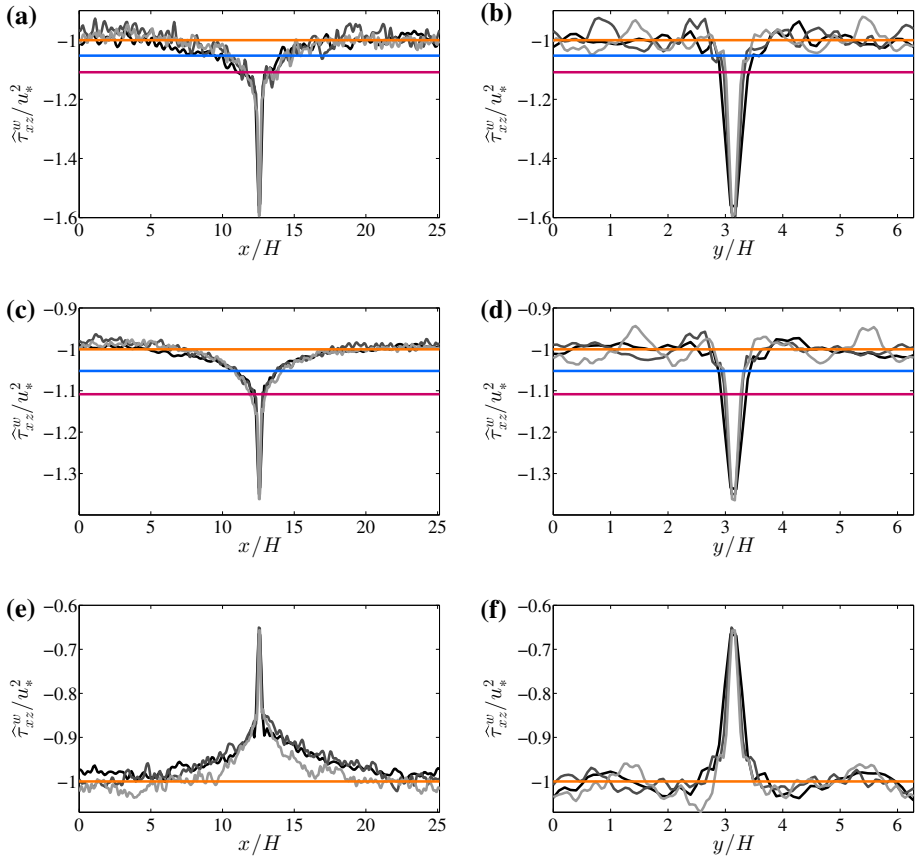


Fig. 8 Transects of conditionally-sampled aerodynamic surface stress, $\hat{\tau}_{xz}^w/u_*^2$, corresponding with thresholds illustrated in Fig. 6: (a,b) $\hat{\tau}_{\alpha,yz}^w(x, y)/u_*^2$; (c,d) $\hat{\tau}_{\beta,yz}^w(x, y)/u_*^2$; and (e,f) $\hat{\tau}_{\gamma,yz}^w(x, y)/u_*^2$. Orange marker denotes location of threshold stress. Contours correspond with case LES3 in Table 1. Panels (a,c,e) retrieved from transverse position, $y/H = \pi$; panels (b,d,f) retrieved from streamwise position, $x/H = 4\pi$. On panels (a,b,c,d), solid blue and red contours correspond with candidate values of non-dimensional threshold stress, $u_*^2 \lambda^{-2} = 1.05$ and $u_*^2 \lambda^{-2} = 1.108$, respectively

Fig. 8 shows profiles for $\hat{\tau}_{\alpha,yz}^w(x, y)/u_*^2$, $\hat{\tau}_{\beta,yz}^w(x, y)/u_*^2$, and $\hat{\tau}_{\gamma,yz}^w(x, y)/u_*^2$ for cases LES1, LES2, and LES3.

The profiles in Fig. 8 are illuminating in terms of showing how the conditionally-sampled surface stress peaks radially tend towards the plane-average value, $\langle \tau_{xz}^w \rangle_{xy}/u_*^2 = -1$ (horizontal, orange line in Fig. 8), distal to the sampling point. The profiles appear to exhibit resolution-invariance, although recall the $\tau_{xz}^w(x_c, y_c, t) \rangle_{xy}/u_*^2$ p.d.f.s that show how low-resolution cases fail to capture some of the extreme events. Moreover, the profiles provide a clearer indication of the ‘region of influence’ associated with extreme stress. Consider first Fig. 8a, b, c and d, which correspond with $\hat{\tau}_{\alpha,yz}^w(x, y)/u_*^2$ and $\hat{\tau}_{\beta,yz}^w(x, y)/u_*^2$, respectively. It is clear that the profile is streamwise asymmetric, wherein local surface-stress peaks occur simultaneously with elevated stress upwind (with a more rapid tendency to $\langle \tau_{xz}^w \rangle_{xy}/u_*^2 = -1$ downwind of the sampling point). The stress profiles are symmetric about the sampling point in the transverse direction. Both trends point to the morphology of coherent, high-momentum

regions above the sampling site and responsible for the region of elevated stress. Moreover, the streamwise extent, $10 \lesssim x/H \lesssim 15$, is of the scale reported for large-scale motions (3–5 channel or boundary-layer depths). As per the Fig. 7c contour, the Fig. 8e $\hat{\tau}_{y,yz}^w(x, y)/u_*^2$ profile is streamwise asymmetric. Unlike the Fig. 8a, b, c, and d profiles, here the streamwise asymmetry of $\hat{\tau}_{y,yz}^w(x, y)/u_*^2$ is such that the low-stress region has greater streamwise extent in the downwind direction [consistent with a conceptual model for smooth walls proposed by (Sheng et al. 2009)]. Finally, the Fig. 8f transverse profile clearly shows the signature of flanking high-momentum regions.

In Sect. 1.1, the non-dimensional threshold, λ , was defined as a means to compare ambient ABL forcing against a given landscape aeolian saltation threshold. For $\lambda > 1$, the ABL can mobilize sediments, and it was reasoned that—for $\lambda < 1$ —variations in u_* associated with turbulence would be exclusively responsible for saltation. This integrates with results presented in this section, where conditionally-sampled stress (Eqs. 12–14 and Fig. 6) is shown to correlate closely with the presence of large- and very-large-scale motions. To conclude this section, a series of candidate values for $u_{*,t}$ and u_* (based on realistic conditions) are introduced. Equation 3 has been used to estimate $u_{*,t}$ with $A_B = 0.2$ [the high $Re_{*,t}$ value; (Shao 2008)], $\rho_a = 1.2745 \text{ kg m}^{-3}$, $\rho_p = 2650 \text{ kg m}^{-3}$, and $D_p = 200 \mu\text{m}$ [i.e. relatively large sediment grains mobilized via the saltation and drift transport modes; (Shao 2008; Kok et al. 2012)]. These Eq. 3 input arguments yield $u_{*,t} = 0.404 \text{ m s}^{-1}$. Equation 5 has been used to estimate the ABL friction velocity, $u_{*,a}$, with $U_G = 9.5$ and 9.75 m s^{-1} , $H_G = 100 \text{ m}$ (representative surface layer elevation), and $z_0 = 0.005 \text{ m}$ [the value used in this study and representative of a flat, minimally vegetated landscape that may be susceptible to aeolian activity with diminishing soil moisture; (Holliday 2001; Stout 2007, 2010; Lanigan et al. 2015)]. These Eq. 5 input arguments yield $u_{*,a} = 0.38$ and 0.39 m s^{-1} . Note the change of nomenclature here for ABL friction velocity, $u_{*,a}$, which is needed since u_* has been used to denote the LES pressure gradient forcing (see also Sect. 2). The non-dimensional stress shown in Figs. 7 and 8 can be re-scaled to identify specific values of stress associated with threshold exceedence via multiplication with the product, $[u_*(u_{*,t}/u_{*,a})]^2 = u_*^2\lambda^{-2}$, which for the aforementioned Eqs. 3 and 5 input arguments yields $u_*^2\lambda^{-2} = 1.05$ and 1.108 . Of course, different input arguments produce different values for λ , but the values selected here are entirely within the realms of physical reality and therefore apropos to demonstration that large-scale motions are important to aeolian activity. To finalize this discussion, profiles of $u_*^2\lambda^{-2}$ have been superimposed on Fig. 7a, b and 8a–d, which illustrates how the spatial extent of conditionally-sampled stress correlates with the silhouette of $u_*^2\lambda^{-2}$. The large spatial extent of these simulations can give the misleading conclusion that the threshold contours on Fig. 7a and b are ‘small’ ellipses surrounding the sampling point, but in fact the $u_*^2\lambda^{-2} = 1.05$ and 1.108 contours are $\approx 4H$ and $2H$ in length. Similarly, the Fig. 8a–d transects show how aeolian saltation would be concentrated within the footprint of these large structures based on the selected candidate thresholds.

3.5 Conditionally-Averaged Flow

Figures 9 and 10 show the conditionally-averaged flow field in streamwise and transverse vertical planes, respectively, for case LES1. We show visualization for case LES1 since this particular simulation was run for the longest duration (Table 1 indicates $T U_0 H^{-1} \approx 12,000$), and therefore the conditionally-sampled flow for this case is most smooth. Note, however, the Fig. 8 transects, which demonstrate that all simulations reveal the spatial footprint of these large-scale structures. Figure 9a and b show the fluctuating conditionally-averaged

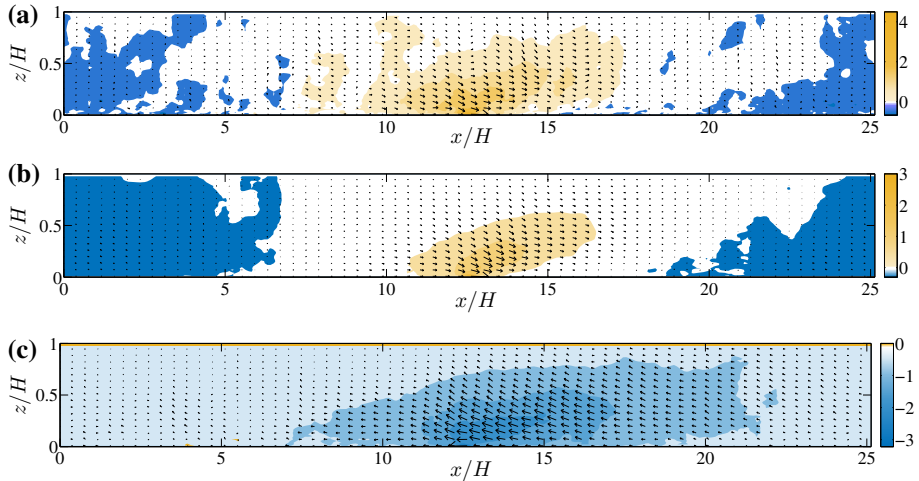


Fig. 9 Visualization of case LES1 conditionally-sampled flow field, \hat{u}/u_* , in the x - z plane corresponding with thresholds illustrated in Fig. 6: **a** \hat{u}_α/u_* ; and **b** \hat{u}_β/u_* ; and **c** \hat{u}'/u_* . Contour shows \hat{u}'/u_* , vectors show $\{\hat{v}'/u_*, \hat{w}'/u_*, \hat{u}'/u_*, \hat{w}/u_*, \hat{v}/u_*\}$, where vector lengths have been globally increased for illustration purposes. Orange marker denotes location of threshold stress. Vertical plane retrieved from transverse position, $y/H = \pi$

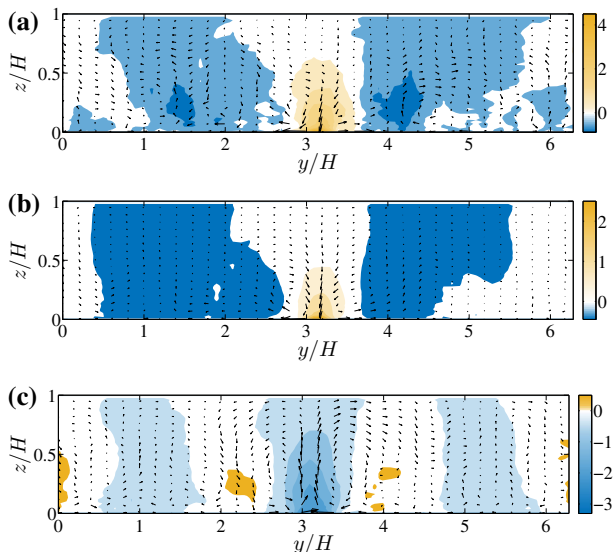


Fig. 10 Visualization of case LES1 conditionally-sampled flow field, \hat{u}/u_* , in y - z plane corresponding with thresholds illustrated in Fig. 6: **a** \hat{u}_α/u_* ; and **b** \hat{u}_β/u_* ; and **c** \hat{u}'/u_* . Contour shows \hat{u}'/u_* , vectors show $\{\hat{v}'/u_*, \hat{w}'/u_*, \hat{u}'/u_*, \hat{w}/u_*, \hat{v}/u_*\}$, where vector lengths have been globally increased for illustration purposes. Vertical plane retrieved from streamwise position, $x/H = 4\pi$

streamwise velocity contour during high stress events at the sampling point (see Eqs. 9 and 10). As was apparent from Figs. 7 and 8, elevated surface stress at the sampling point occurs simultaneously with elevated stress over a region. Figure 9a and b show that, indeed, during elevated stress there is a streamwise momentum excess (relative to the plane-average), or

high-momentum region; visible with the contour. Moreover, the vector fields show that the elevated stress corresponds with a negative vertical velocity. The streamwise extent of the high-momentum region is $10 \lesssim x/H \lesssim 15$, or approximately five domain depths. Similarly, Fig. 10a and b shows visualization of \hat{u}_α/u_* and \hat{u}_β/u_* in the transverse vertical plane, which clearly demonstrates ‘downwelling’ above the sampling site and evidence of counter-rotating, streamwise-aligned vortical flows flanking the high-momentum region (with positive and negative sign corresponding with downwelling, or $\hat{w}/u_* < 0$). In contrast, during the relatively low stress events, contours of \hat{u}'_y/u_* indicate a large streamwise momentum deficit above the sampling site (with streamwise extent exceeding the qualitatively observed values for \hat{u}'_α/u_* and \hat{u}'_β/u_* ; below, this is confirmed with correlation contours). In the streamwise vertical plane (Fig. 9c), this is accompanied by ‘upwelling’, or $\hat{w}/u_* > 0$. In the transverse vertical plane, Fig. 10c shows the presence of counter-rotating, streamwise-aligned vortices (with sign opposite to that corresponding with \hat{u}_α/u_* and \hat{u}_β/u_* , and showing upwelling above the test site).

For all thresholds, the contours of \hat{u}'_α/u_* , \hat{u}'_β/u_* , and \hat{u}'_y/u_* , show an inclination in the streamwise vertical plane with angle, θ , upwind of the sampling site that is comparable to the instantaneous observations (Fig. 2a). This also suggests that extreme surface stress values are associated with the passage of coherent (large- and very-large-scale motions) momentum excesses and deficits in the outer, inertial layer. The conditionally averaged flow fields therefore indicate that aeolian saltation will exhibit spatial heterogeneity, where the spatial footprint is controlled by the morphology of coherent, turbulent structures present in the atmospheric surface layer.

3.6 Spatial Cross-Correlations

The spatial attributes of the conditionally-averaged flow fields (Eqs. 9–11) have been determined, where contours of the conditionally-averaged fluctuating streamwise velocity are shown as,

$$R_{\hat{u}'\hat{u}'}(z; z_{\text{Ref.}}) = \frac{\langle \hat{u}'(x, z)\hat{u}'(x, z_{\text{Ref.}}) \rangle_x}{\langle \hat{u}(x, z)^2 \rangle_x^{1/2} \langle \hat{u}(x, z_{\text{Ref.}})^2 \rangle_x^{1/2}}, \quad (15)$$

where $\langle \hat{u}(x, z)^2 \rangle_x^{1/2}$ is the root-mean-square of $\hat{u}(x, z)$, averaged in x , and $z_{\text{Ref.}}$ is a pre-defined reference elevation.

Here, $z_{\text{Ref.}}/H = 0.0078$, which ensures that the maximum value of $R_{\hat{u}'\hat{u}'}(z; z_{\text{Ref.}})$ occurs when $z/H \approx 0.0078$ (this is apparent from inspection of Fig. 11). Figure 11a, c, and e show contours of $R_{\hat{u}'\hat{u}'}(z; z_{\text{Ref.}})$ for thresholds α , β , and γ , respectively; all contours illustrate a positive spatial lag that is the signature of streamwise-inclined coherent structures (Hutchins et al. 2012; Chauhan et al. 2013; Anderson et al. 2015). The contours are completely consistent with the Fig. 9 visualizations, showing that \hat{u}'_α/u_* and \hat{u}'_β/u_* exhibit a smaller streamwise correlation than \hat{u}'_y/u_* . The streamwise extent of these conditionally sampled, positively inclined [in the streamwise-vertical plane], structures is computed as,

$$\delta x(z; z_{\text{Ref.}}) = \arg \max_{\delta x} (R_{\hat{u}'\hat{u}'}(z; z_{\text{Ref.}})(\delta x)). \quad (16)$$

In order to simplify the presentation of $\delta x(z; z_{\text{Ref.}})$, a model for $\delta x^*(z; z_{\text{Ref.}})$ is shown, which is an error-minimized linear profile for $\delta x(z; z_{\text{Ref.}})$. Orange profiles for $\delta x^*(z; z_{\text{Ref.}})$ are shown in Fig. 11a, c, and e; the profiles overlap with positions of maximum correlation. Both $\delta x(z; z_{\text{Ref.}})$ and $\delta x^*(z; z_{\text{Ref.}})$ have been used to compute the inclination angle,

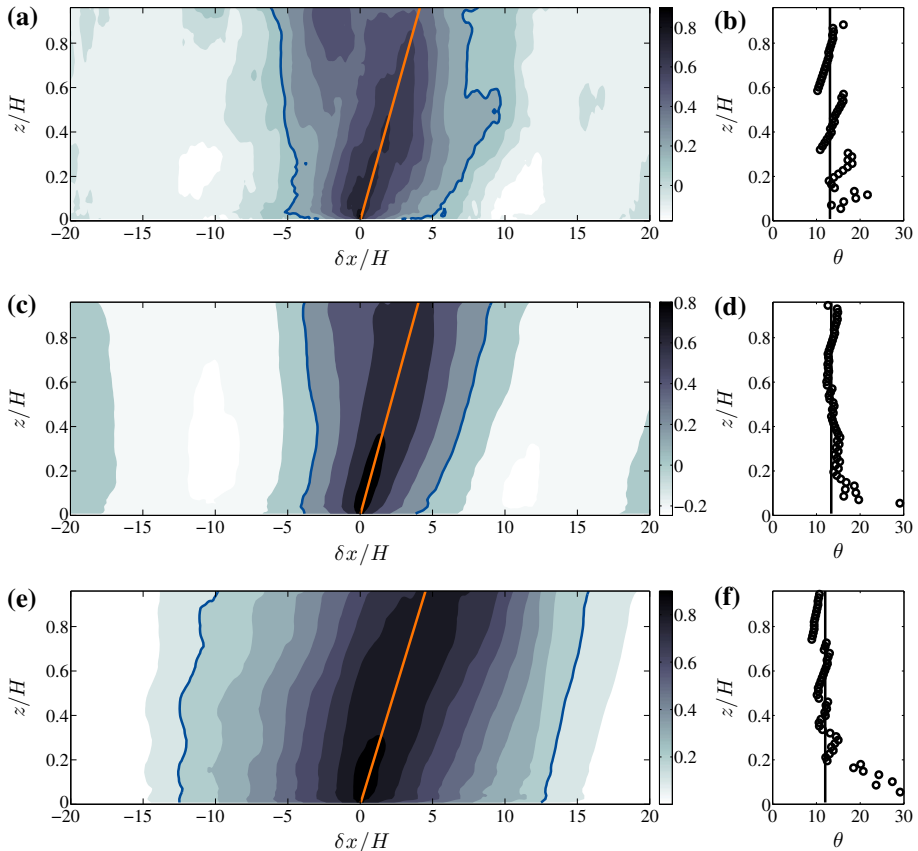


Fig. 11 Visualization of case LES1 turbulence structural attributes: panels (a,c,e) show the two-point correlation of \hat{u}' ; panels (b,d,f) show the structural inclination angle, θ . Panels (a,b), (c,d), and (e,f) show statistics for \hat{u}_α/u_* , \hat{u}_β/u_* , and \hat{u}_γ/u_* , respectively. On panels (a,c,e), orange line denotes error-minimized model fit to spatial lag, $\delta x(z; z_{\text{Ref.}})$ (see also Eq. 16), while blue lines denote $R_{\hat{u}' \hat{u}'}(z; z_{\text{Ref.}}) = 0.2$ (for illustration). On panels (b,d,f), solid line shows error-minimized model fit for inclination angle, $\theta^*(z)$, while symbols are based on conditionally sampled flow field, $\theta(z)$ (see also Eq. 17)

$$\theta(z) = \frac{\delta z}{\delta x(z; z_{\text{Ref.}})}, \quad (17a)$$

$$\theta^*(z) = \frac{\delta z}{\delta x^*(z; z_{\text{Ref.}})}. \quad (17b)$$

Figure 11b, d, and f show $\theta^*(z)$ and $\theta(z)$ for thresholds α , β , and γ , as indicated in the caption. The modelled profile value is a constant, $\theta^*(z) \approx 13^\circ$, for all thresholds, which is in agreement with values reported for the ABL (Chauhan et al. 2013). For γ , the LES datapoints deviate slightly from the model value for $z/H \lesssim 0.2$, which is a product of low N_γ (see Sect. 3.3 and Eqs. 11 and 14). Nonetheless, for all cases, it is clear that the spatial attributes of flow structures present during extreme values of surface stress resemble large-scale motions.

4 Conclusion

Large-eddy simulation has been used to model neutrally-stratified turbulent ABL flow over a flat landscape with low aerodynamic roughness length (a configuration designed to replicate ambient conditions present in flows over arid, desert-like landscapes) (Holliday 2001; Stout 2007, 2010). A computational domain with streamwise extent, $L_x/H = 8\pi$, was used to ensure that all scales of turbulence (in the context of LES) were resolved, from sub- H motions associated with mechanical shear in the near-wall region to large-scale and very-large-scale motions (this was confirmed with a spectrogram of the fluctuating streamwise velocity component) in the outer layer (Hutchins and Marusic 2007a). Conditional averaging predicated on extreme high and low surface stress has been used to characterize the large-scale structural nature of turbulence during such events, where selection of pre-defined ‘high’ and ‘low’ stress was based on a posteriori p.d.f. of stress. The p.d.f. was negatively skewed, with extreme events that are statistically infrequent but physically important for aeolian processes, since mobilization of dust and sediments is driven by imposed (aerodynamic) surface stress.

Thus, through use of a computational domain with significant streamwise extent and carefully-selected threshold, extreme surface stress has been associated with specific attributes of the flow. Results presented herein, conditionally-averaged flow and surface stress, \hat{u} and $\hat{\tau}_{xz}^w$, all comprehensively show that extreme surface stress is associated with the passage of large-scale motions. That is, the passage of large-scale motions (whether composed of uniformly low or uniformly high momentum fluid) corresponds with statistically infrequent surface stresses. This is important for aeolian processes, since large-scale motions are flanked by large-scale counter-rotating streamwise vortices and uniformly positive (low-momentum region) or negative (high-momentum region) vertical velocity fluid. Thus, once suspended, dust and sediments are exposed to complex ‘transport pathways’ associated with dynamics of the large-scale motion. In order to properly demonstrate relevance of this work for characterizing aeolian morphodynamics, a non-dimensional ratio, λ , quantifying the ABL’s capacity to induce aeolian saltation was defined. Numerical values of λ were estimated using candidate values for threshold friction velocity and ABL friction velocity (based on realistic input arguments), and enabled the authors to relate the conditionally sampled stress to the threshold.

Since the results presented have demonstrated the extent to which the spatial attributes of large- and very-large-scale motions can serve as a control on aeolian morphodynamics, it is of further interest to identify any conditions that may alter the spatial attributes of these structures. One such condition is thermal stratification, which changes constantly in the ABL over the diurnal cycle and greatly alters turbulence dynamics and spatial attributes of coherent structures. During the evening hours, when buoyancy inhibits production of turbulence by mechanical shear, aeolian processes are subdued (owing to a smaller u_* associated with intermittent and smaller vertical velocity fluctuations). In contrast, during daytime hours, turbulence is produced simultaneously via surface heating (turbulent plumes) and mechanical shear. It has been definitively shown that aeolian processes exhibit a strong diurnal dependence (Stout 2007, 2010; Lanigan et al. 2015), owing to the ambient thermal gradients and their role in the production of turbulence. Moreover, a recent study by Chauhan et al. (2013) has shown that the inclination angle, θ , is negatively correlated with the Obukhov length (i.e., enhanced surface heating results in steepening of large-scale motions). We are presently working to characterize the structural attributes of coherent large-scale motions subjected to surface heating (unstable stratification), to elucidate how the dynamics of such structures affect aeolian saltation.

Acknowledgments We thank anonymous reviewers for providing comprehensive, insightful comments that led to a much improved final manuscript. This work was supported by the National Science Foundation (Program Manager: Drs. N. Anderson, C. Lu, and E. Bensman) under Award No. AGS-1500224 (and Summer 2015 REU Supplement Award No. AGS-1542855), and by the University of Texas at Dallas (startup support). Computational resources were provided by the Texas Advanced Computing Center at the University of Texas at Austin. The authors thank David Lanigan and John Stout for helpful comments.

References

- Adrian R (1988) Linking correlations and structure: stochastic estimation and conditional averaging. In: Zaric ZP (ed) Memorial international seminar on near-wall turbulence, Hemisphere
- Ahn J, Lee J, Lee J, Kang JH, Sung H (2015) Direct numerical simulation of a $30r$ long turbulent pipe flow at $Re_\tau = 3008$. *Phys Fluids* 27(065):110
- Albertson J, Parlange M (1999) Surface length scales and shear stress: implications for land-atmosphere interaction over complex terrain. *Water Resour Res* 35:2121–2132
- Anderson W (2015) Amplitude modulation of streamwise velocity fluctuations in the roughness sublayer: evidence from large-eddy simulations. *J Fluid Mech* 789:567–588
- Anderson W, Chamecki M (2014) Numerical study of turbulent flow over complex aeolian dune fields: The White Sands National Monument. *Phys Rev E* 89:1–14
- Anderson W, Meneveau C (2010) A large-eddy simulation model for boundary-layer flow over surfaces with horizontally resolved but vertically unresolved roughness elements. *Boundary-Layer Meteorol* 137:397–415
- Anderson W, Meneveau C (2011) A dynamic large-eddy simulation model for boundary layer flow over multiscale, fractal-like surfaces. *J Fluid Mech* 679:288–314
- Anderson W, Li Q, Bou-Zeid E (2015) Numerical simulation of flow over urban-like topographies and evaluation of turbulence temporal attributes. *J Turbul* 16:809–831
- Antonia R (1981) Conditional sampling in turbulence measurement. *Annu Rev Fluid Mech* 13:131–156
- Baas A (2006) Wavelet power spectra of aeolian sand transport by boundary layer turbulence. *Geophys Res Lett* 33(L05):403
- Baas A (2008) Challenges in aeolian geomorphology: investigating aeolian streamers. *Geomorphology* 93:3–16
- Bagnold R (1937) The transport of sand by wind. *Geogr J* 89(5):409–438
- Bagnold R (1956) The physics of blown sand and desert dunes. Chapman and Hall, London
- Bai K, Meneveau C, Katz J (2012) Near-wake turbulent flow structure and mixing length downstream of a fractal-tree. *Boundary-Layer Meteorol* 143:285–308
- Bailey B, Stoll R (2013) Turbulence in sparse, organized vegetative canopies: a large-eddy simulation study. *Boundary-Layer Meteorol* 147:369–400
- Balakumar B, Adrian R (2007) Large- and very-large-scale motions in channel and boundary-layer flows. *Philos Trans R Soc* 365:665–681
- Belcher S, Harman I, Finnigan J (2012) The wind in the willows: flows in forest canopies in complex terrain. *Annu Rev Fluid Mech* 44:479–504
- Bohm M, Finnigan J, Raupach M (2000) Dispersive fluxes and canopy flows: Just how important are they? In: Proceedings of the 24th conference on agricultural and forest meteorology, American Meteorology Society, Davis, pp 106–107
- Bou-Zeid E, Meneveau C, Parlange M (2005) A scale-dependent lagrangian dynamic model for large eddy simulation of complex turbulent flows. *Phys Fluids* 17(025):105
- Brutsaert W (2005) Hydrology: an introduction. Cambridge University Press, Cambridge 605 pp
- Calaf M, Meneveau C, Meyers J (2010) Large-eddy simulation study of fully developed wind-turbine array boundary layers. *Phys Fluids* 22(015):110
- Calaf M, Parlange M, Meneveau C (2011) Large eddy simulation study of scalar transport in fully developed wind-turbine array boundary layers. *Phys Fluids* 23(126):603–616
- Castro I (2007) Rough-wall boundary layers: mean flow universality. *J Fluid Mech* 585:469–485
- Chauhan K, Hutchins N, Monty J, Marusic I (2013) Structure inclination angles in the convective atmospheric surface layer. *Boundary-Layer Meteorol* 147:41–50
- Cheng H, Castro I (2002) Near wall flow over urban-like roughness. *Boundary-Layer Meteorol* 104:229–259
- Chester S, Meneveau C, Parlange M (2007) Modelling of turbulent flow over fractal trees with renormalized numerical simulation. *J Comput Phys* 225:427–448

- Coccol O, Dobre A, Thomas TG, Belcher S (2007) Structure of turbulent flow over regular arrays of cubical roughness. *J Fluid Mech* 589:375–409
- Deardorff J (1972) Numerical investigation of neutral and unstable planetary boundary layers. *J Atmos Sci* 29:91–115
- Dennis D, Nickels T (2011a) Experimental measurement of large-scale three-dimensional structures in a turbulent boundary layer. Part 1. Vortex packets. *J Fluid Mech* 673:180–217
- Dennis D, Nickels T (2011b) Experimental measurement of large-scale three-dimensional structures in a turbulent boundary layer. Part 2. Long structures. *J Fluid Mech* 673:218–244
- Dupont S, Alfaro S, Bergametti G, Marticorena B (2015) Near-surface dust flux enrichment in small particles during erosion events. *Geophys Res Lett* 42:1992–2000
- Fang J, Porté-Agel F (2015) Large-eddy simulation of very-large-scale motions in the neutrally stratified atmospheric boundary layer. *Boundary-Layer Meteorol* 155:397–416
- Finnigan J, Shaw R, Patton E (2009) Turbulence structure above a vegetation canopy. *J Fluid Mech* 637:387–424
- Ganapathisubramani B, Longmire EK, Marusic I (2003) Characteristics of vortex packets in turbulent boundary layers. *J Fluid Mech* 478:35–46
- Garratt JR (1994) The atmospheric boundary layer. Cambridge University Press, Cambridge 316 pp
- Germano M (1992) Turbulence: the filtering approach. *J Fluid Mech* 238:325–336
- Germano M, Piomelli U, Moin P, Cabot W (1991) A dynamic subgrid-scale eddy viscosity model. *Phys Fluids* 3:1760–1765
- Graham J, Meneveau C (2012) Modeling turbulent flow over fractal trees using renormalized numerical simulation: alternate formulations and numerical experiments. *Phys Fluids* 24(125):105
- Grant S, Marusic I (2012) Crossing turbulent boundaries: interfacial flux in environmental flows. *Environ Sci Technol* 45:1443–1453
- Grass A (1971) Structural features of turbulent flow over smooth and rough boundaries. *J Fluid Mech* 50:233
- Harmon I, Finnigan JJ (2007) A simple unified theory for flow in the canopy and roughness sublayer. *Boundary-Layer Meteorol* 123:339–364
- Hellström L, Ganapathisubramani B, Smits A (2015) The evolution of large-scale motions in turbulent pipe flow. *J Fluid Mech* 779:701–715
- Holliday V (2001) Stratigraphy and geochronology of upper quaternary eolian sand on the southern High Plains of Texas and New Mexico, United States. *Bull Geol Soc Am* 113:88–108
- Hong J, Katz J, Meneveau C, Schultz M (2012) Coherent structures and associated subgrid-scale energy transfer in a rough-wall channel flow. *J Fluid Mech* 712:92–128
- Hutchins N, Marusic I (2007a) Evidence of very long meandering features in the logarithmic region of turbulent boundary layers. *J Fluid Mech* 579:1–28
- Hutchins N, Marusic I (2007b) Large-scale influences in near-wall turbulence. *Philos Trans R Soc A* 365:647–664
- Hutchins N, Nickels T, Marusic I, Chong M (2009) Hot-wire spatial resolution issues in wall-bounded turbulence. *J Fluid Mech* 635:103–136
- Hutchins N, Monty J, Ganapathisubramani B, Ng H, Marusic I (2011) Three-dimensional conditional structure of a high-reynolds-number turbulent boundary layer. *J Fluid Mech* 673:255–285
- Hutchins N, Chauhan K, Marusic I, Monty J, Klewicki J (2012) Towards reconciling the large-scale structure of turbulent boundary layers in the atmosphere and laboratory. *Boundary-Layer Meteorol* 145:273–306
- Jimenez J (2004) Turbulent flow over rough wall. *Annu Rev Fluid Mech* 36:173
- Kim J, Moin P, Moser R (1987) Turbulence statistics in fully-developed channel flow at low reynolds-number. *J Fluid Mech* 177:133–166
- Kim K, Adrian R (1999) Very large-scale motion in the outer layer. *Phys Fluids* 11:417–422
- Klewicki J, Metzger M, Kelner E, Thurlow E (1995) Viscous sublayer flow visualizations at $r_\theta \approx 1500000$. *Phys Fluids* 7:857–863
- Kok J, Parteli E, Michaels T, Karam D (2012) The physics of wind-blown sand and dust. *Rep Prog Phys* 75(106):901
- Krogstad P, Antonia R (1999) Surface roughness effects in turbulent boundary layers. *Exp Fluids* 27:450–460
- Krogstad P, Antonia R, Browne L (1992) Comparison between rough and smooth-wall turbulent boundary layers. *J Fluid Mech* 245:599617
- Lanigan D, Stout J, Anderson W (2015) Atmospheric stability and diurnal patterns of aeolian saltation on the Llano Estacado. *Aeolian Res* 21:131–137
- Martin RL, Barchyn TE, Hugenholtz CH, Jerolmack DJ (2013) Timescale dependence of aeolian sand flux observations under atmospheric turbulence. *J Geophys Res Atmos* 118:9078–9092
- Marusic I, Mathis R, Hutchins N (2010) Predictive model for wall-bounded turbulent flow. *Science* 329:193–196

- Mason P, Thomson D (1987) Large-eddy simulations of the neutral-static-stability planetary boundary layer. *Q J R Meteorol Soc* 113:413–443
- Mathis R, Hutchins N, Marusic I (2009) Large-scale amplitude modulation of the small-scale structures in turbulent boundary layers. *J Fluid Mech* 628:311–337
- Mathis R, Hutchins N, Marusic I (2011) A predictive inner-outer model for streamwise turbulence statistics in wall-bounded flows. *J Fluid Mech* 681:537–566
- Mathis R, Marusic I, Chernyshenko S, Hutchins N (2013) Estimating wall-shear-stress fluctuations given an outer region input. *J Fluid Mech* 715:163–180
- Meinhart C, Adrian R (1995) On the existence of uniform momentum zones in a turbulent boundary layer. *Phys Fluids* 7:694–696
- Meneveau C, Katz J (2000) Scale-invariance and turbulence models for large-eddy simulation. *Annu Rev Fluid Mech* 32:1–32
- Moeng CH (1984) A large-eddy-simulation model for the study of planetary boundary-layer turbulence. *J Atmos Sci* 41:2052–2062
- Pahtz T, Kok J, Herrmann H (2012) The apparent roughness of a sand surface blown by wind from an analytical model of saltation. *New J Phys* 14(043):035
- Raupach M, Antonia R, Rajagopalan S (1991) Rough-wall turbulent boundary layers. *Appl Mech Rev* 44:1–25
- Reynolds JF, Smith DMS, Lambin EF, Turner BL, Mortimore M, Batterbury SPJ, Downing TE, Dowlatabadi H, Fernndez RJ, Herrick JE, Huber-Sannwald E, Jiang H, Leemans R, Lynam T, Maestre FT, Ayarza M, Walker B (2007) Global desertification: building a science for dryland development. *Science* 316:847–851
- Richter D, Sullivan P (2014) Modification of near-wall coherent structures by inertial particles. *Phys Fluids* 26(103):304
- Schultz M, Flack K (2009) Turbulent boundary layers on a systematically-varied rough wall. *Phys Fluids* 21(015):104
- Shao Y (2008) Physics and modelling of wind erosion. Springer, New York 456 pp
- Sheng J, Malkiel E, Katz J (2009) Buffer layer structures associated with extreme wall stress events in a smooth wall turbulent boundary layer. *J Fluid Mech* 633:17–60
- Stevens R, Wilczek M, Meneveau C (2014) Large-eddy simulation study of the logarithmic law for second- and higher-order moments in turbulent wall-bounded flow. *J Fluid Mech* 757:888–907
- Stout J (2007) Simultaneous observations of the critical aeolian threshold of two surfaces. *Geomorphology* 85:3–16
- Stout JE (2010) Diurnal patterns of blowing sand. *Earth Surf Process Landf* 35:314–318
- Tennekes H, Lumley J (1972) A first course in turbulence. MIT Press, Cambridge
- Thomas D, Knight M, Wiggs G (2005) Remobilization of southern african desert dune systems by twenty-first century global warming. *Nature* 453:1218–1221
- Townsend AA (1976) The structure of turbulent shear flow. Cambridge University Press, Cambridge
- Volino R, Schultz M, Flack K (2007) Turbulence structure in rough- and smooth-wall boundary layers. *J Fluid Mech* 592:263–293
- Wu Y, Christensen KT (2007) Outer-layer similarity in the presence of a practical rough-wall topology. *Phys Fluids* 19(085):108
- Wu Y, Christensen KT (2010) Spatial structure of a turbulent boundary layer with irregular surface roughness. *J Fluid Mech* 655:380–418
- Wyngaard JC (1979) The planetary boundary. World Meteorological Organization, Technical Note 165, Ed McBean, WMO-No 530, Geneva
- Wyngaard JC (2010) Turbulence in the atmosphere. Cambridge University Press, Cambridge 201 pp
- Xie ZT, Coceal O, Castro I (2008) Large-eddy simulation of flows over random urban-like obstacles. *Boundary-Layer Meteorol* 129:1–23